Evolution of the Electronic Band Structure and Efficient Photo-Detection in Atomic Layers of InSe

Sidong Lei,[†] Liehui Ge,[†] Sina Najmaei,[†] Antony George,[†] Rajesh Kappera,[‡] Jun Lou,[†] Manish Chhowalla,[‡] Hisato Yamaguchi,[§] Gautam Gupta,[§] Robert Vajtai,[†] Aditya D. Mohite,[§,*] and Pulickel M. Ajayan[†,*]

[†]Department of Materials Science and NanoEngineering, Rice University, Houston, Texas 77005, United States, [‡]Department of Materials Science, Rutgers, the State University of New Jersey, Piscataway, New Jersey 08854, United States, and [§]MPA-11 Materials Synthesis and Integrated Devices, Los Alamos National Laboratory, Los Alamos, New Mexico 87545, United States

ABSTRACT

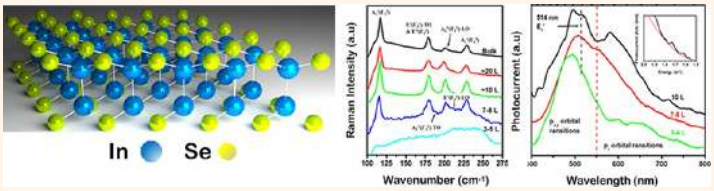

Atomic layers of two-dimensional (2D) materials have recently been the focus of extensive research. This follows from the footsteps of graphene, which has shown great potential for ultrathin optoelectronic devices. In this paper, we present a comprehensive study on the synthesis, characterization, and thin film photodetector application of atomic layers of InSe. Correlation between resonance Raman spectroscopy and photoconductivity measurements allows us to systematically track the evolution of the electronic band structure of 2D InSe as its thickness approaches few atomic layers. Analysis of photoconductivity spectra suggests that few-layered InSe has an indirect band gap of 1.4 eV, which is 200 meV higher than bulk InSe due to the suppressed interlayer electron orbital coupling. Temperature-dependent photocurrent measurements reveal that the suppressed interlayer interaction also results in more localized p_z-like orbitals, and these orbitals couple strongly with the in-plane E′ and E″ phonons. Finally, we measured a strong photoresponse of 34.7 mA/W and fast response time of 488 μs for a few layered InSe, suggesting that it is a good material for thin film optoelectronic applications.

KEYWORDS: photodetector · 2D layered materials · resonance Raman scattering · InSe · photoconductivity

Transformation of a material from bulk to two-dimensional (2D) results in the realization of new physical phenomena. The resulting properties form the basis for futuristic thin film technologies. Since the discovery of graphene from bulk graphite in 2004,[1] it has been viewed as an ideal material for next generation applications in photonics, nonlinear optics, THz electronics, flexible transparent electrodes, sensors, conductive composites, and gas separation membranes.[2−10] Despite extensive studies,[11−16] graphene-based FETs still cannot compete with traditional silicon-based electronic devices as it suffers from an intrinsic bottleneck for its use in optoelectronic applications. Graphene is a zero band gap semiconductor in which the conduction and valence bands meet at the Fermi energy. This implies that there are no electronic states in graphene that allow photoexcited carriers to be generated and have long enough lifetimes[17,18] to develop optoelectronic devices such as photodetectors and photovoltaics. Although some reports showed graphene has photoresponse and responsivity is high, the dark current is usually very high due the absent of band gap.[19−21] Despite these shortcomings, graphene research has served as a catalyst for the birth of a new field, beyond graphene, in the form of novel 2D layered semiconducting materials also known as transition-metal dichalcogenides (TMDC) that exhibit novel electrical and optical properties.[22−32] Recent studies have shown that single-layer MoS_2 has a photoresponsivity of 0.42 mA/W and a band gap of 1.8 eV.[33] Lopez-Sanchez *et al.* showed that the photoresponsivity of MoS_2 can be significantly enhanced by

* Address correspondence to amohite@lanl.gov, ajayan@rice.edu.

Received for review August 29, 2013 and accepted January 6, 2014.

Published online January 06, 2014
10.1021/nn405036u

achieving lower resistance contacts.[34] Although it has advantages in form factor for its use as an ultrathin photodetector, the band gap is relatively large and does not overlap well with the visible spectrum, making it intrinsically nonideal for its use as an active element for visible light photodetector applications.

Besides TMDC, several III−VI group van der Waals layered structures materials such as GaS,[35] GaSe,[36,37] and In_2Se_3[38] have also been studied as layered photoresponse matierals. Because of their dramatic photoresponse and large nonlinear effect, these bulk materials have been widely used in the areas of photodetection, nonlinear optics, and THz generation source.[39−42] The photoresponse of mechanically exfoliated[37,43] and synthetic few layered GaSe[36] exhibits good photoresponse with low dark currents and an external quantum efficiency. However, both theoretical[44] and experimental[36] work has shown that the band gap of GaSe changes dramatically (from 1.8 to 3.2 eV) with decreasing number of layers, which originates from the suppressed interlayer interactions from the p_z-like orbitals of Se atoms. Therefore, these devices have a weak photoresponse in the visible region. On the other hand, InSe, another III−VI layered semiconductor with a band structure similar to GaSe has a narrower band gap[42,45] with a near perfect overlap with the visible spectrum and is expected to outperform the above-mentioned layered 2D materials.

In this paper, we present an extensive study on (a) synthesis and isolation (b) optical and electrical properties (25 to 250 K) and (c) ultrathin photodetector application of few-layered InSe. Direct correlation between resonance Raman spectra and the photoconductivity reveals a systematic evolution of the 2D band structure from bulk to few layered InSe. Detailed analyses of photoconductivity spectra show that few-layered InSe has an indirect band gap of 1.4 eV. The 200 meV difference compared to 1.2 eV for bulk InSe is due to the suppression of interlayer coupling as its thickness approaches a few atomic layers. Temperature-dependent measurements on a few layered InSe devices reveal the signature of localized electronic states that couple strongly to the in-plane E′ and E″ phonons. Furthermore, we demonstrate that few layered InSe is an good candidate for thin film photodetector application with a photoresponsivity of 34.7 mA/W and a response time of 488 μs.

RESULT AND DISCUSSION

The crystal structure of InSe is consists of In−Se−Se−In layers as depicted in Figure 1a. The distance between two neighboring layers is 0.84 nm, and the lattice constant along the axes is 0.40 nm.[46] Each layer has hexagonal structure as shown in Figure 1b and has a D_{3h} symmetry.

The crystals synthesized with In−Se nonstoichiometric melt[46] according to the phase diagram[47] have a black mica-like texture with a layered morphology. Energy dispersive X-ray spectrum (EDX) showed an indium to selenium ratio of 1:1 (refer to Supporting Information, Figure S1). We also performed high-resolution transmission electron microscopy (HRTEM) to characterize the crystal structure and evaluate the overall crystalline quality of the exfoliated InSe sample. Few layered 2D samples of InSe for HRTEM were prepared by chemical exfoliation. The bulk InSe crystals were sonicated in Dimethylformamide (DMF) for 48 h and drop casted on to a lacy carbon TEM grid. Figure 1c illustrates the HRTEM image of InSe, which shows perfect hexagonal lattice structure of the synthesized material. The lattice constant measured along (100) direction gives a value of 0.40 nm, which is in agreement with the reported lattice constant of InSe.[46] The selected area electron diffraction pattern is shown in Figure 1d and presents a 6-fold symmetry, which is an indicator of the overall crystalline quality, thus confirming that the synthesized InSe has a good crystal structure and justifies its use as the starting material for the investigation of the optical and electrical properties of few layered InSe.

A few layers of InSe flakes were obtained by using the mechanical exfoliation technique established by Novoslov and co-workers for the isolation of graphene from HOPG.[1] Briefly, the bulk crystal is peeled with tweezers into pieces with a diameter of 4−5 mm and a thickness of tens of micrometers. Few-layered InSe flakes, tens of micrometers in size, were mechanically exfoliated using scotch tape and optically visualized after transferring on a silicon wafer with 285 nm thermally grown SiO_2 layer. The atomic force microscope (AFM) was used to measure the thickness and roughness of the exfoliated InSe flake on top of SiO_2. Parts a and b of Figure 2 show the AFM topography images and the corresponding optical images of typical samples studied here. The thickness of the exfoliated samples typically varied from 4 to 10 nm, which corresponds to 4−11 atomic layers. The exfoliated top surface was extremely flat along the cleavage plane of InSe crystal, suggesting weak van der Waals coupling between the layers.

In order to probe the electronic band structure and lattice vibration properties of InSe, Raman measurements (resonance and nonresonant) were performed on a few layered InSe flakes. Resonance Raman process involves the transitions between actual electronic energy levels, so in addition to probing lattice vibrations (or phonons), it can also provide insights into electronic states in InSe. Consistent with previous studies on bulk InSe, an argon line (514 nm) laser was used to excite the resonant Raman transition in InSe that arises from interband E_1' transition (energy difference of 2.4 eV originating between the p_x,p_y-like orbitals to the bottom of the conduction band[42,48]) and is illustrated in Figure 3 with green arrows. Nonresonant Raman transition is represented as red arrows between the p_x,p_y-like orbitals to some virtual energy level such that the

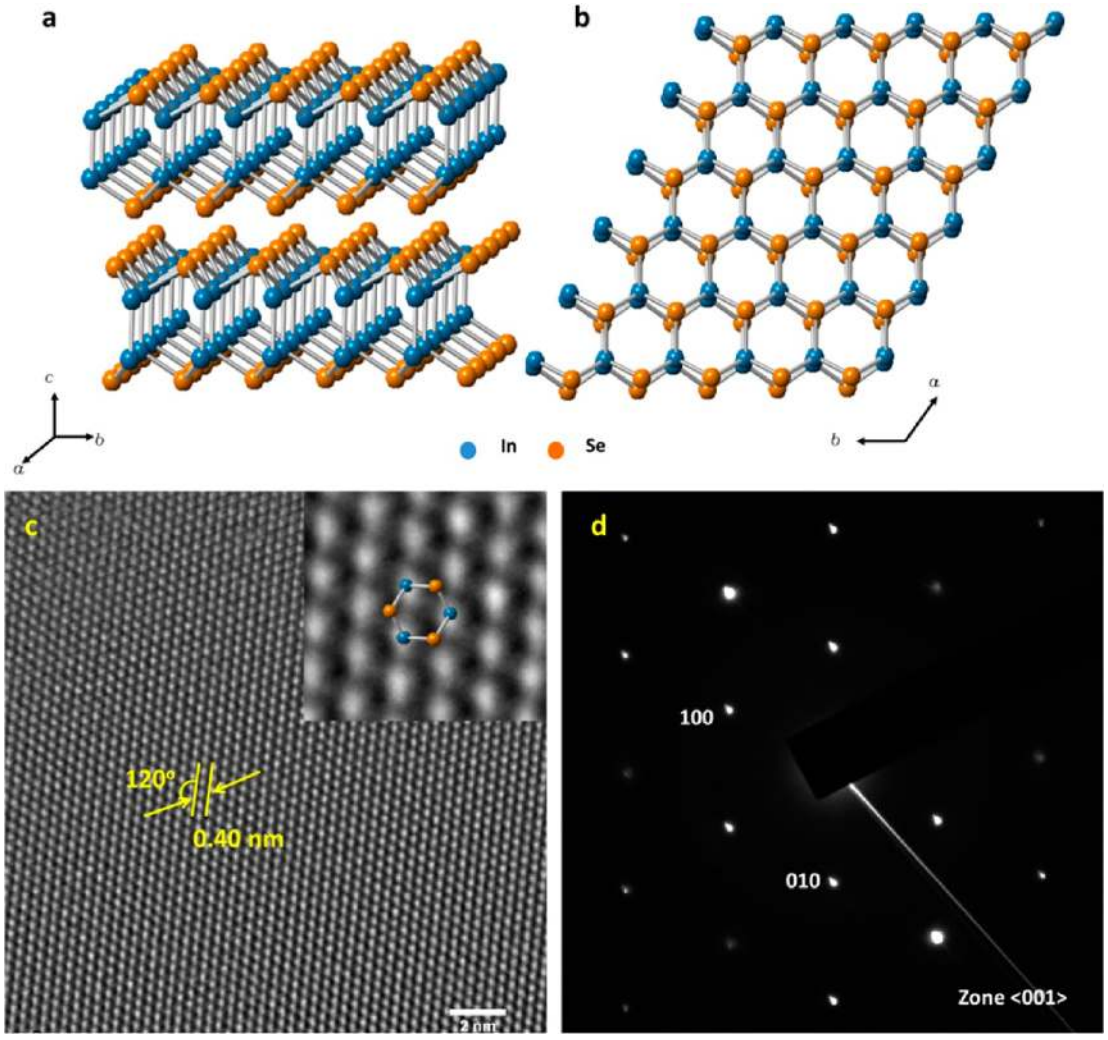

Figure 1. Crystal structure of InSe. The blue spheres refer to Indium atoms and the brown spheres refer to the selenium atoms. (a) Side view of the lattice structure, the distance between two neighboring layers is 0.84 nm. The top-view shown in (b) has a hexagonal structure with single layer symmetry of D_{3h}; the lattice constant along *a* or *b* axis is 0.40 nm. High-resolution TEM image of InSe flake (c) and electron-beam diffraction pattern (d). The lattice constant along a axes is measured (100) direction as shown in (c) and reads a value of 0.40 nm. The electron-beam diffraction pattern is collected with an electron-beam shined along c axes. The diffraction pattern shows a 6-fold symmetry, which indicates good crystal quality.

energy difference is lower than resonant Raman energy of 2.4 eV.

The resonant (laser excitation 514 nm) and nonresonant (laser excitation 633 nm) Raman spectra are shown in parts b and c, respectively, of Figure 4. The following discussion assumes that the sample is mainly ε-InSe or (and) γ-InSe, as the Raman spectra agree well with previous studies on bulk ε-InSe and γ-InSe crystals.[49] The Mulliken symbols are used to label the corresponding ε-InSe vibration modes (ε-InSe has the same point group symmetry to single InSe layer, so all the discussion about ε-InSe can also be applied to single InSe layer) and the Γ symbols are used to label the vibration modes in γ-InSe consistent with previous work on bulk InSe.[49] In each unit cell of ε-InSe, there are two layers of *Se*−*In*−*In*−*Se* atomic unit, i.e., eight atoms in each unit cell. Counting the three degrees of freedom for each atom, it has 24 vibrational modes. Since ε-InSe has D_{3h} symmetry, it has four A_2'' modes, four A_1'' modes, eight E′ modes, and eight E″ modes. In γ-InSe, each unit cell has 12 atoms and, consequently, 36 vibration modes. In C_{3v} symmetry, they are divided into 12 Γ_1 modes and 24 Γ_3 modes. Experimentally, we observed seven modes (the reason for the observation of limited number of modes is discussed in Supporting Information).

The Raman modes (see Figure 4a) observed in resonant Raman (see Figure 4b) and nonresonant Raman (see Figure 4c) are listed in Table 1. We observed seven modes in our resonant Raman spectrum, $A_1'(\Gamma_1^2)$ at 117 cm^{-1}, $E'(\Gamma_3^1)$-TO and $E''(\Gamma_3^3)$ at 179 cm^{-1}, $A_2''(\Gamma_1^1)$-TO at 187 cm^{-1}, $A_2''(\Gamma_1^1)$-LO at 201 cm^{-1}, $E'(\Gamma_3^1)$-LO at 212 cm^{-1} ,and $A_1'(\Gamma_1^3)$ at 227 cm^{-1}. In contrast, the nonresonant Raman only shows the A_1' (Γ_1^2) mode at 117 cm^{-1}, $E'(\Gamma_3^1)$-TO and $E''(\Gamma_3^3)$ modes at 179 cm^{-1}, and $A_1'(\Gamma_1^3)$ mode at 227 cm^{-1} because other modes

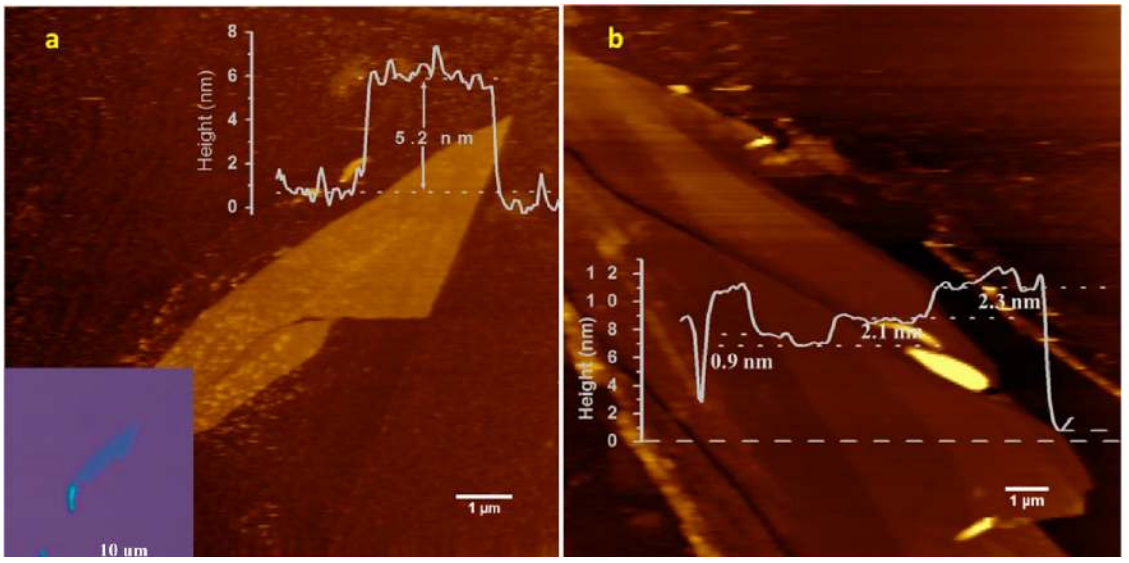

Figure 2. AFM image of exfoliated InSe flakes. (a) Flake with a thickness of 5.2 nm, which corresponds to four to five layers. (b) Thinner flake with varying thickness. The thickness of the flake varies from 6 to 12 nm, with a step height of 2 nm, which corresponds to two layers.

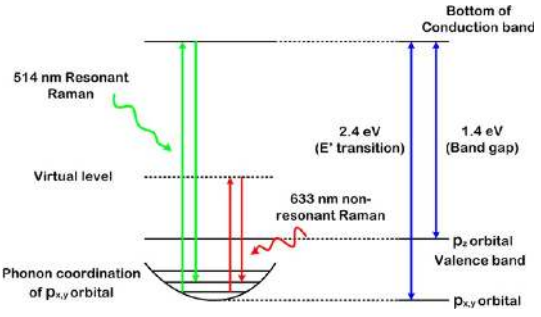

Figure 3. Electronic band structure and Raman processes in few-layered InSe flakes. The band gap of InSe is defined between p_z like orbitals, which forms the top of the valence band and the bottom of the conduction band. The transition between the $p_{x,y}$ orbital to bottom of the conduction band (E_1' transition) corresponds to an energy gap of 2.4 eV (514 nm). A laser excitation with 514 nm results in the resonant Raman process, while excitation with a 633 nm laser line gives a nonresonant Raman process.

are forbidden by Raman selection rules, relatively weak or are degenerate in energy (E″ and E′-TO mode are degenerate in energy). We also observed a Rayleigh tail (the broad background in the spectrum) in the resonant Raman pattern, which results from the fluorescence accompanying the resonant process. This phenomenon was not observed in the nonresonant Raman pattern (flat background).

From the resonant and nonresonance Raman measurements we estimate (a) the number of layers of InSe and (b) changes in the electronic band structure of InSe from bulk to few layers. The number of layers of InSe can be estimated from the ratio of $A_2''(\Gamma_1^1)$-LO and $E'(\Gamma_3^1)$-TO peaks, as illustrated in the Raman mapping (see Figure 4e).

For bulk InSe, the resonant $A_2''(\Gamma_1^1)$-LO peak at 201 cm^{-1} is relatively weak, and the $A_2''(\Gamma_1^1)$ -TO and LO branches of $E'(\Gamma_3^1)$-LO mode were not observed. As the number of layers decreases, the intensity of $A_2''(\Gamma_1^1)$ mode does not decrease as dramatically as the other peaks. Thus, these changes in the relative peak intensity of $A_2''(\Gamma_1^1)$-LO can be used as a reference to estimate the number of layers of InSe. Parts d and e of Figure 4 show the correlated optical image of one InSe flake and variation of thickness across the flake, and the corresponding Raman mapping that shows the relative peak intensity of A_2'' (Γ_1^1) -LO peak (ratio between $A_2''(\Gamma_1^1)$-LO and $E'(\Gamma_3^1)$-TO). It is clear that the thicker regions give lower intensity, while the $A_2''(\Gamma_1^1)$-LO mode is much stronger in thinner regions. For the resonance Raman spectra all peaks are clearly detectable for flakes that are ~7 layers and above, which is in sharp contrast to nonresonant Raman spectra where only A_1' mode was observed at 227 cm^{-1}. However, as the number of layers decreases to three to five layers, all the Raman peaks (resonant and nonresonant) disappear leaving behind a broad envelope indicated by the blue curve in Figure 4b. The observation of the resonance Raman peaks up to ~7 layers suggests the energy gap between p_x,p_y-like orbitals and the bottom of the conduction band (see Figure 3) does not change appreciably for up to ~7 layers. However, as the number of layers becomes less than ~7 layers, both p_z orbital the $p_{x,y}$-like orbitals should strongly be affected by the suppressed interlayer coupling and result in observable changes in the electronic band structure that lead to the disappearance of the resonance Raman peaks.

To directly probe the changes in the electronic band structure and to understand the disappearance of Raman modes with the decreasing number of layers of InSe, we performed photoconductivity experiments, which are illustrated in Figure 5a. InSe metal−semiconductor−metal

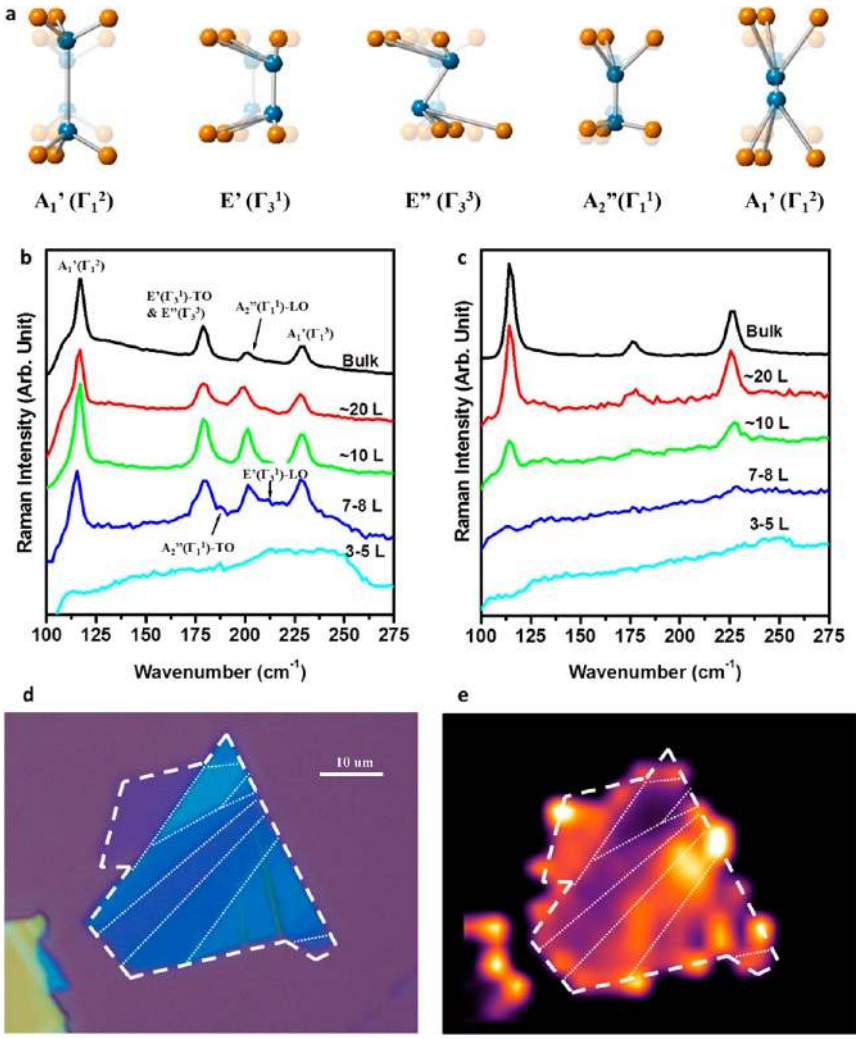

Figure 4. Raman studies of mechanically exfoliated InSe flakes. (a) Observed vibrational modes in our study. The E′ mode and A_2'' are spilt into LO and TO modes, respectively, due to the coupling between lattice vibration and electromagnetic field. (b) Thickness-dependent resonant Raman spectra of InSe flakes with a 514 nm argon ion laser excitation. As a reference, the nonresonant Raman spectra were taken with a 633 nm excitation (c). The peak intensity ratio between $A_2''(\Gamma_1^1)$-TO and $E'(\Gamma_3^1)$-TO was used to estimate the number of layers. An optical image of InSe flake with variant thickness (d) used for Raman maps shown in (e). The ratio of the peak intensities reveals that as the number of layers decreases, the ratio becomes higher.

TABLE 1. Resonant Raman (Different Layers) and Nonresonant Raman Modes Observed in InSe Flakes

mode	$A_1'(\Gamma_1^2)$	$E'(\Gamma_3^1)$-TO and $E''(\Gamma_3^3)$	A_2'' (Γ_1^1)-TO	A_2'' (Γ_1^1)-LO	$E'(\Gamma_3^1)$-LO	$A_1'(\Gamma_1^3)$
resonant						
bulk	117	179		201		227
~20 L	117	179		199		228
~10 L	117	179		201		227
7−8 L	115	179	187	201	212	227
nonresonant						
>10 L	117	179				227

(MSM) photodetector devices were fabricated on layered InSe flakes with different thicknesses, with Ti/Au (10 nm/30 nm) electrodes. Figure 5a captures the changes in the photocurrent spectra as a function of the number of layers of InSe. The red dashed line separates the spectra into two parts. The left part (400 to 550 nm), corresponds to the electronic transition from $p_{x,y}$-like orbital (referred to as *xy*-band in the following discussion) to the bottom of conduction band, and the right part (550 to 800 nm, refer to z-band in the following discussion) corresponds to electronic transition from p_z-like orbitals to the bottom of conduction band. As the number of layers goes down below ~7 layers, the photocurrent response in the z-band decreases sharply. This is because the interaction between p_z-like orbitals (which is perpendicular to the layer plane) in neighboring layers is strongly suppressed. This is consistent with measurements on GaSe[36] that have the same crystal structure. In addition, we also observe that the E_1' peak in the *xy*-band arising from $p_{x,y}$-like orbital to conduction band experiences a strong blue shift of ~150−200 meV shifting the E_1' transition energy from 2.41 eV (λ~514 nm)

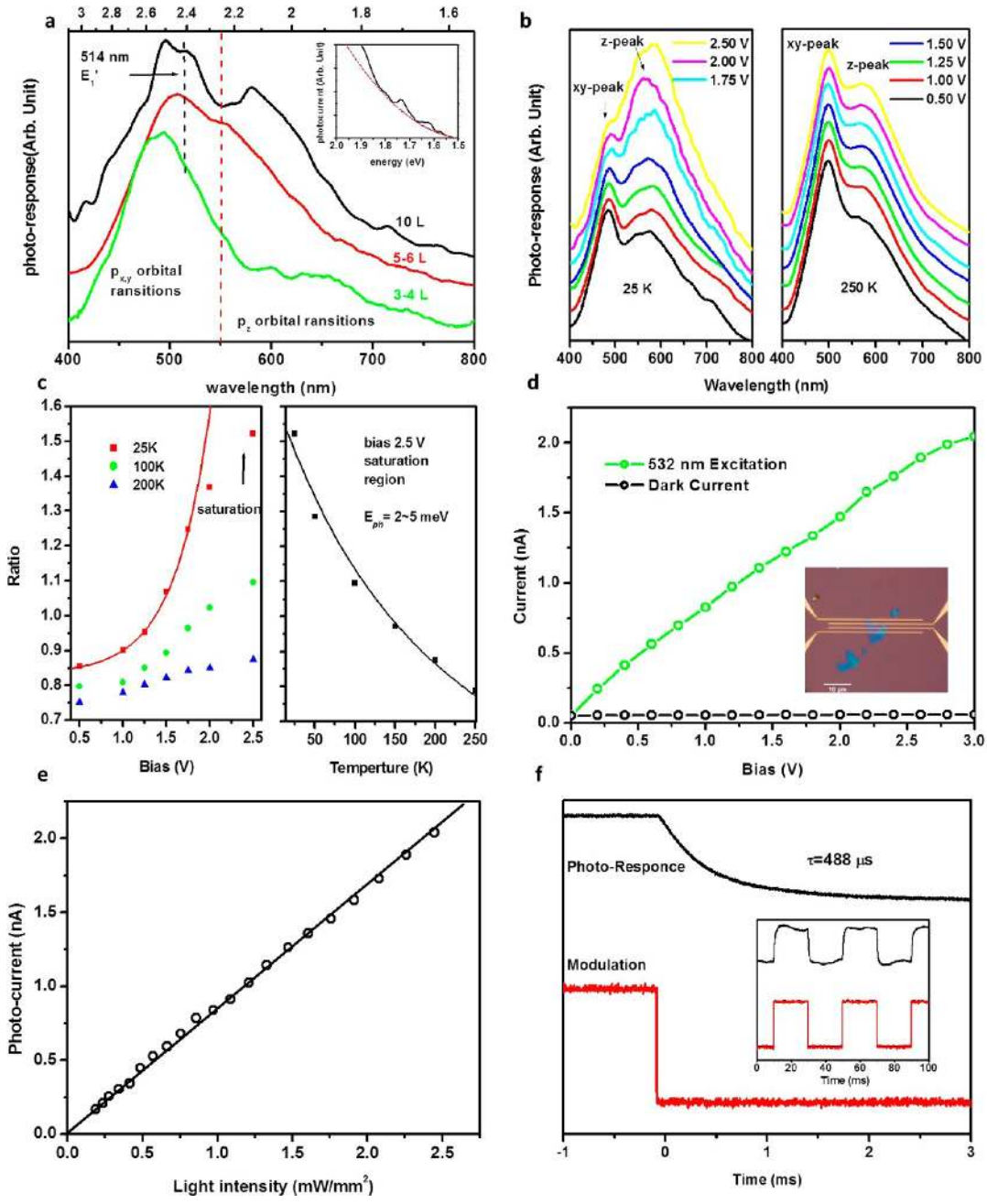

Figure 5. Photocurrent response of InSe metal−semiconductor−metal photodetector. (a) Photoresponse spectra of 10 layer, 7−8 layer, and 3−4 layer samples. The red dash line separates the spectra into two parts: p_z-orbital transition (right) and $p_{x,y}$-obrital E_1' transition (left). The black dashed line indicates the 514 nm E_1' transition. As the number of layers decrease, the photoresponse in the p_z-orbital transition region is suppressed, while the $p_{x,y}$-obrital E_1' transition experience a blue shift. Inset to (a) shows the fit to the tail with a parabola suggesting that few-layered InSe is an indirect band gap semiconductor with a band gap of 1.4 eV. Left part of (b) shows photoresponse with different bias voltage under 25 K and right part shows photoresponse with different bias voltage under 250 K. Left part of (c) shows ratio between p_z-peak to $p_{x,y}$-peak as a function of bias voltage at different temperature. (red square: 25 K, green dot: 100K, blue triangle: 200 K). The red curve is fitting by exponential function. Right part of (c) show the ratio between p_z-peak to $p_{x,y}$-peak as a function of temperature at 2.5 V bias. The black curve is fitting curve using the equation (*). (d) Current−voltage curve under dark and light conditions. Inset to (d) shows the optical image of the device used for measuring the photodetector response. Excitation power was 2.5 mW/mm^2 with a 532 nm laser that gives a responsivity of 34.7 mA/W and a quantum efficiency of 8.1%. The device shows a good linear response as the light intensity changes (e) with a linear dynamic rang larger than 46.5 dB. The response time of the device is measured from the decay curve (f) and gives a value of 488 μs.

to ~2.6 eV (480 nm). This blue shift in the E_1' transition with decreasing number of layers is consistent with the disappearance of the Raman modes. Resonance Raman modes can no longer be excited with a 514 nm laser line and leads to the disruption of the resonance Raman process and subsequent vanishing of the Raman peaks for few-layered InSe as illustrated in Figure 4b.

We also extracted the band gap of a multilayered InSe from the shape of the measured photocurrent spectra for a 10 layered device (see the black curve in Figure 5a). It was difficult to extract band-gaps for thinner layers (7−8 and 3−4) due to the lack of a clear band-edge in the photocurrent spectra (the distribution of the density of electron states in thinner samples will be discussed later in the manuscript). We observed that the photocurrent spectra decayed gradually with increasing wavelength, suggesting that the few-layered InSe has an indirect band gap. This is in sharp contrast to a direct band gap semiconductor where the photocurrent is expected to turn off sharply below the band gap of the material. By assuming that the internal quantum efficiency of photocurrent (I_{ph}) is a constant in the 700−800 nm range, the photocurrent is proportional to the absorption in this wavelength range, i.e., $I_{ph} = \alpha \times d \times \eta$, where α is the absorption, d is the thickness of the InSe flake, and η (quantum efficiency) is a constant. For indirect band gap semiconductors the following equation applies:

$$\alpha \propto (E - E_g)^{1/2}$$

Therefore

$$I_{ph} \propto (E - E_g)^{1/2}$$

(Here, we assume that the absorption rate $1 - e^{-\alpha d}$ can be expressed as αd for thin films). By fitting the spectrum edge, as shown in the inset of Figure 5a, we extract a band gap of around 1.4 eV. This phenomenon is similar to few-layered GaSe,[36] but the strength of the interlayer interaction is not as strong as GaSe, where, as the number of layers decreases, the coupling due to the p_z-like orbitals vanishes, leading to an effective band gap of 3.26 eV.[36] Thus, the correlation between resonance Raman spectroscopy and photoconductivity measurements allows us to track the changes in the electronic band structure of InSe with decreasing number of layers.

As mentioned above, for thinner samples (below 7 layers), we do not observe a clear band-edge. This suggests that electronic density of states is much less in thinner samples in the spectral region corresponding to the z-band. The electron states in z-band transform from a continuous energy band to localized and isolated states due to the disappearance of interlayer interaction. If this is true, then the contribution to photocurrent due to the z-band should have a strong temperature and bias dependence. Hence, to test our hypothesis and understand the nature of the localized states and electron−phonon interaction, we performed temperature and bias dependent photocurrent measurements on few atomic layered (seven to eight layers) InSe flakes in MSM device geometry (see Figure 5b,c). Figure 5b shows the bias dependence of the photocurrent spectra plotted as a function of excitation wavelength at 250 and 25 K. The data clearly suggest that the photocurrent contribution originating from the xy-band and z-band behave quite differently as a function of bias voltage and temperature (the spectra are normalized to the E_1' peak in xy-band). At lower temperatures (25 K), as we increase the bias voltage, the relative intensity of photocurrent in z-band increases dramatically in comparison to xy-band (see the left panel of Figure 5b). The field dependence supports the view that the states in z-bands are localized and a large electrical field works to delocalize and dissociate the electron−hole pairs[50] converting them into free carriers that contribute to the photocurrent. For temperature (250 K, right panel of Figure 5b), the relative intensity of z-band does not change appreciably with increasing bias suggesting that a strong electron−phonon interaction in z-band suppresses the overall photocurrent. To quantitatively estimate the localization energy and electron−phonon interaction, we describe below a model that provides an excellent agreement with experimental results. Figure 5c captures the ratio between z-band peak and xy-band peak as a function of bias voltage (left panel of Figure 5c) and temperature, respectively (right panel of Figure 5c).

To extract the electron localization energy, we consider the photocurrent ratio measured for a temperature of 25 K and ignore the higher temperature photocurrent response to avoid the contribution from phonon scattering. As can be observed (left panel Figure 5c), the ratio (z-peak/xy-peak) increases sharply as a function of bias voltage and begins to saturate for biases >2 V. In the lower bias region, the photocurrent ratio of z-peak to xy-peak can be expressed as a simple exponential formula given by

$$\text{ratio} = \alpha e^{-(\beta V - \varphi)/kT}$$

where, α is coefficient for fitting, φ refers to the localization energy of electron in z-band, βV refers to the ionization energy imposed by the applied electrical field, and k is Boltzmann constant. This gives an excellent fitting to the data in the low bias region, measured at 25 K and is shown by the red curve. We extract an electron localization energy, φ = 7 meV suggesting that the electron excitation is localized with a barrier height of 7 meV in z-band and the photoexcited charge carriers can be delocalized by applying a large enough electrical field.

We used the high field region (≥2.0 V) to investigate the electron−phonon interaction independent of the electron localization effect under the assumption that at high electric fields all of the electrons are delocalized and merely the interaction between electron and phonon dominates. Figure 5c (right panel) shows the ratio of z-peak to xy-peak as a function of temperature at constant bias voltage. To describe the behavior, we build the following model. After the optical generation and delocalization of electron−hole pairs by an electrical field, two processes can happen: (a) photocurrent

generation where the electron can recombine with the hole through the external circuit or (b) recombination process in which the electrons can get trapped back into the localized state accompanying the emission or absorption of a phonon. The recombination process can be mathematically expressed as

$$\frac{dN}{dt} = -\frac{N}{\tau_{ph}} = -\xi N_{ph} N \quad (1)$$

where ξ is the electron−phonon interaction coefficient, N_{ph} is the number of phonons, and N is the number of electrons. The photocurrent process can also be treated as a carrier losing process and can be expressed as

$$-\frac{I_{z\text{-band}}}{\varepsilon(T)} = \frac{dN}{dt} = -\frac{N}{\tau_{ef}} \quad (2)$$

$\varepsilon(T)$ represents other thermal processes, such as interband electron−hole recombination, *etc.*, and these processes have the same effects on both excitations in the z-band and xy-band. τ_{ef} is a time constant describing the charge carrier propagating process and can be express as

$$\tau_{ef} = \frac{\eta d}{\mu E} = \frac{\eta d^2}{\mu V} \quad (3)$$

where, η is a constant, d is the spacing between electrodes, μ is the mobility of electrons, E is the electrical field, and V is bias voltage across electrodes. Thus, the entire process by combining eqs 1−3 be expressed as

$$\frac{dN}{dt} = -\frac{N}{\tau_{ef}} - \frac{N}{\tau_{ph}} + \zeta N_{hv} \quad (4)$$

where ζN_{hv} is the number of electrons generated by radiation. In the steady state, considering the Bose−Einstein distribution of phonons, the photocurrent intensity of the z-peak can be expressed as

$$I_{z\text{-band}} = \varepsilon(T)\zeta N_{hv} \times \frac{e^{E_{ph}/kT} - 1}{e^{E_{ph}/kT} - 1 + \frac{\xi\eta d^2}{\mu V}} \quad (5)$$

Considering the photocurrent in the xy-band is also proportional to $\varepsilon(T)$, the ratio can be expressed as

$$\text{ratio} = \frac{I_{z\text{-band}}}{I_{xy\text{-band}}} \propto \zeta N_{hv} \times \frac{e^{E_{ph}/kT} - 1}{e^{E_{ph}/kT} - 1 + \frac{\xi\eta d^2}{\mu V}} \quad (6)$$

The above formula was applied to fit the ratio verses temperature data under 2.5 V bias and is illustrated in the right panel of Figure 5c. The black curve shows the fitting and reveals E_{ph} has value of 2−5 meV, which corresponds to the in-plane E′ (16 cm^{-1}, 2 meV) or/and E″ (40 cm^{-1}, 5 meV) vibrational modes,[49] which are out of range for our Raman setup. From the above result we conclude that, in the z-band, the localized electron states are mainly effected by E′ or/and E″ phonons. This is reasonable, as in 2D structure, electrons are only allowed to have interactions with in-plane phonons because of conservation of momentum. Meanwhile, the barrier height of the localized state (7 meV) is in the same order of phonon energy, so that the conservation of energy can be easily met. Considering that the localized states should have zero momentum, and the momentum of the phonon involved in this process is very small, it is instructive to speculate that the process occurs near the center of Brillouin zone, *i.e.*, Γ point.

We also measured the photodetector response and critical figures of merit for a few layered InSe in the visible region and the results are illustrated in Figure 5d−f. These were collected from the device (number of layers ∼10) shown in the inset of Figure 5d. Figure 5d shows the current−voltage curve of the device with an effective exposure area of 23 μm^2 measured in the dark and with a 532 nm laser with an intensity of 2.5 mW/mm^2. The dark current (I_{dk}) is in the order of 10 pA, which is at the detection limit of the current amplifier used for our measurements. The photocurrent is 2 nA with a 3 V bias, corresponding to an on/off ratio of 200, a photoresponsivity (($I_{ph} - I_{dk}$)/light intensity) of 34.7 mA/W, and an external quantum efficiency of 8.1%. The intensity response of InSe few-layered flake MSM photodetector is shown in Figure 5e. Up to 2.5 mW/mm^2, the InSe few-layered MSM photodetector maintained a good linear response, with a linear dynamic range (= 20 log (I_{ph}/I_{dk})) larger than 46.5 dB. We also measured a response time of 488 μs (Figure 5f), which is an order of magnitude faster than that measured on MoS_2.

These figures of merit suggest that few-layered InSe is good for low noise photo detection in the visible region. In comparison with GaSe (grown by vapor phase transport) device having similar contact material and device configuration, and measured under the same experimental conditions,[36] the photoresponsivity and quantum efficiency of InSe is higher and the linear dynamic range is better.[37] It also worth to notice that the responsivity of InSe may be further improved by improving the contact configuration, which has been observed in MoS_2 (from 0.42 mA/W[33] to 880A/W[34]) and GaSe (from 17 mA/W[36] to 2.8 A/W[37]). More importantly, InSe has a smaller band gap than GaSe[36] and MoS_2,[51] hence, stronger visible light response, and at the same time, the response speed of InSe device is much faster. These intrinsic advantages make few layered InSe a more promising material for ultrathin visible light photodetection.

CONCLUSION

In summary, we provide a comprehensive study of synthesis, characterization and optoelectronic application of atomic layered InSe. Direct correlation between resonance Raman spectroscopy and photoconductivity measurements allows us to systematically track the

evolution of the 2D electronic band structure of InSe as we approach few layers. Temperature-dependent photocurrent measurements and theoretical modeling suggests that E′ and E″ phonon couple the localized electronic states arising from the p_z-like orbitals. Further, we demonstrate that few layered InSe has an extremely strong photoresponse and is an excellent 2D material for its incorporation as an ultrathin photodetector with a high photoresponsivity of 34.7 mA/W and fast response time of 488 μs. By optimization the contact with an appropriate metal, the performance of few-layered InSe photodetector may be further enhanced.

METHODS

Crystal Synthesis. The synthesis of bulk InSe crystal was performed by using a nonstoichiometric melt of indium (>99.99%, Alfa Aesar Co.) and selenium (>99.99%, Sigma-Aldrich Co.). Indium and selenium were mixed with a molar ratio of 52:48[46] and sealed in a quartz tube under vacuum (10^{-3} Torr). The precursor was then heated to 685 °C, and the temperature was maintained for 3 h to ensure a full reaction between indium and selenium. Further, in accordance to the phase diagram of In−Se system,[47] the temperature was increased to 700 °C and maintained for 3 h to form a uniform InSe melt. The melt was then cooled down to 500 °C at a ramp rate of 10 °C per hour, followed by natural cooling to room temperature in 6 h to achieve InSe crystals with high quality.

Photoconductivity Measurement. The photoconductivity was performed in Janis probe-station with liquid helium cryo-stat. For I−V measurement, a 532 nm laser with a beam size of 0.5 mm diameter was applied to the device, and the I−V curve was measured with Keithley 2400. For spectrum measurement, the light emerging from monochromator (Newport CornerStone) was led to the sample by multimode optical fiber. The device was powered by Keithley 2400 and current (spectrum) were recorded by oscilloscope after amplified by low-noise current preamplifier (Stanford Research System). The spectrum was normalized to the number of photos.

For time-resolved measurement, the 532 nm laser was modulated by an acoustic optical modulator with a square wave at 500 Hz and then was shined onto the sample. The current output by the device was sent to low-noise current preamplifier before recorded. The current amplifier was set with a DC coupling mode and a bandwidth of 10 kHz.

Conflict of Interest: The authors declare no competing financial interest.

Acknowledgment. This work was supported by the MURI ARO program, grant no. W911NF-11-1-0362, and by FAME, one of six centers of STARnet, a Semiconductor Research Corporation program sponsored by MARCO and DARPA. The research was also supported by the Laboratory Directed Research and Development Program and by CINT at LANL, an affirmative action equal opportunity employer operated by Los Alamos National Security, LLC, for the National Nuclear Security Administration of the U.S. Department of Energy under contract no. DE-AC52-06NA25396.

Supporting Information Available: Additional information on SEM, EDX, and XRD on InSe grown by nonstoichiometric melt and a discussion about Raman spectral mode. This material is available free of charge *via* the Internet at http://pubs.acs.org.

REFERENCES AND NOTES

1. Novoselov, K. S.; Geim, A. K.; Morozov, S. V.; Jiang, D.; Zhang, Y.; Dubonos, S. V.; Grigorieva, I. V.; Firsov, A. A. Electric Field Effect in Atomically Thin Carbon Films. *Science* **2004**, *306*, 666–669.
2. Sun, Z.; Hasan, T.; Torrisi, F.; Popa, D.; Privitera, G.; Wang, F.; Bonaccorso, F.; Basko, D. M.; Ferrari, A. C. Graphene Mode-Locked Ultrafast Laser. *ACS Nano* **2010**, *4*, 803–810.
3. Bao, Q.; Zhang, H.; Ni, Z.; Wang, Y.; Polavarapu, L.; Shen, Z.; Xu, Q.-H.; Tang, D.; Loh, K. Monolayer Graphene as a Saturable Absorber in a Mode-Locked Laser. *Nano Res.* **2011**, *4*, 297–307.
4. Bao, Q.; Loh, K. P. Graphene Photonics, Plasmonics, and Broadband Optoelectronic Devices. *ACS Nano* **2012**, *6*, 3677–3694.
5. Bunch, J. S.; van der Zande, A. M.; Verbridge, S. S.; Frank, I. W.; Tanenbaum, D. M.; Parpia, J. M.; Craighead, H. G.; McEuen, P. L. Electromechanical Resonators from Graphene Sheets. *Science* **2007**, *315*, 490–493.
6. Vicarelli, L.; Vitiello, M. S.; Coquillat, D.; Lombardo, A.; Ferrari, A. C.; Knap, W.; Polini, M.; Pellegrini, V.; Tredicucci, A. Graphene Field-Effect Transistors as Room-Temperature Terahertz Detectors. *Nat. Mater.* **2012**, *11*, 865–871.
7. Bae, S.; Kim, H.; Lee, Y.; Xu, X.; Park, J.-S.; Zheng, Y.; Balakrishnan, J.; Lei, T.; Ri Kim, H.; Song, Y. I.; *et al.* Roll-to-Roll Production of 30-in. Ggraphene Films for Transparent Electrodes. *Nat. Nanotechnol.* **2010**, *5*, 574–578.
8. Novoselov, K. S.; Falko, V. I.; Colombo, L.; Gellert, P. R.; Schwab, M. G.; Kim, K. A Roadmap for Graphene. *Nature* **2012**, *490*, 192–200.
9. Huang, X.; Zeng, Z.; Fan, Z.; Liu, J.; Zhang, H. Graphene-Based Electrodes. *Adv. Mater.* **2012**, *24*, 5979–6004.
10. Wu, S.; He, Q.; Tan, C.; Wang, Y.; Zhang, H. Graphene-Based Electrochemical Sensors. *Small* **2013**, *9*, 1160–1172.
11. Li, X.; Wang, X.; Zhang, L.; Lee, S.; Dai, H. Chemically Derived, Ultrasmooth Graphene Nanoribbon Semiconductors. *Science* **2008**, *319*, 1229–1232.
12. Zhou, S. Y.; Gweon, G. H.; Fedorov, A. V.; First, P. N.; de Heer, W. A.; Lee, D. H.; Guinea, F.; Castro Neto, A. H.; Lanzara, A. Substrate-Induced Bandgap Opening in Epitaxial Graphene. *Nat. Mater.* **2007**, *6*, 770–775.
13. Hicks, J.; Tejeda, A.; Taleb-Ibrahimi, A.; Nevius, M. S.; Wang, F.; Shepperd, K.; Palmer, J.; Bertran, F.; Le Fèvre, P.; Kunc, J.; *et al.* A Wide-Bbandgap Metal−Semiconductor−Metal Nanostructure Made Entirely from Graphene. *Nat. Phys.* **2012**, *9*, 49–54.
14. Fan, X.; Shen, Z.; Liu, A. Q.; Kuo, J. L. Band Gap Opening of Graphene by Doping Small Boron Nitride Domains. *Nanoscale* **2012**, *4*, 2157–2165.
15. Usachov, D.; Vilkov, O.; Gruneis, A.; Haberer, D.; Fedorov, A.; Adamchuk, V. K.; Preobrajenski, A. B.; Dudin, P.; Barinov, A.; Oehzelt, M.; *et al.* Nitrogen-Doped Graphene: Efficient Growth, Dtructure, and eEectronic Properties. *Nano Lett.* **2011**, *11*, 5401–5407.
16. Shinde, P. P.; Kumar, V. Direct Band Gap Opening in Graphene by BN Doping: Ab Initio Calculations. *Phys. Rev. B: Condens. Matt.* **2011**, *84*.
17. Dani, K.; Lee, J.; Sharma, R.; Mohite, A.; Galande, C.; Ajayan, P.; Dattelbaum, A.; Htoon, H.; Taylor, A.; Prasankumar, R. Intraband Conductivity Response in Graphene Observed Using Ultrafast Infrared-Pump Visible-Probe Spectroscopy. *Phys. Rev. B: Condens. Matt.* **2012**, *86*, 125403.
18. Gilbertson, S.; Dakovski, G. L.; Durakiewicz, T.; Zhu, J.-X.; Dani, K. M.; Mohite, A. D.; Dattelbaum, A.; Rodriguez, G. Tracing Ultrafast Separation and Coalescence of Carrier Distributions in Graphene with Time-Resolved Photoemission. *J. Phys. Chem. Lett.* **2011**, *3*, 64–68.
19. Zhang, B. Y.; Liu, T.; Meng, B.; Li, X.; Liang, G.; Hu, X.; Wang, Q. J. Broadband High Photoresponse from Pure Monolayer Graphene Photodetector. *Nat. Commun.* **2013**, *4*, 1811.
20. Xia, F.; Mueller, T.; Lin, Y. M.; Valdes-Garcia, A.; Avouris, P. Ultrafast Graphene Photodetector. *Nat. Nanotechnol.* **2009**, *4*, 839–843.
21. Mueller, T.; Xia, F.; Avouris, P. Graphene Photodetectors for High-Speed Optical Communications. *Nat. Photonics* **2010**, *4*, 297–301.

22. Li, H.; Yin, Z.; He, Q.; Huang, X.; Lu, G.; Fam, D. W.; Tok, A. I.; Zhang, Q.; Zhang, H. Fabrication of Single and Multilayer MoS_2 Film-Based Field-Effect Transistors for Sensing NO at Room Temperature. *Small* **2012**, *8*, 63–67.
23. Butler, S. Z.; Hollen, S. M.; Cao, L.; Cui, Y.; Gupta, J. A.; Gutiérrez, H. R.; Heinz, T. F.; Hong, S. S.; Huang, J.; Ismach, A. F.; *et al.* Progress, Challenges, and Opportunities in Two-Dimensional Materials Beyond Graphene. *ACS Nano* **2013**, *7*, 2898–2926.
24. Gutiérrez, H. R.; Perea-López, N.; Elías, A. L.; Berkdemir, A.; Wang, B.; Lv, R.; López-Urías, F.; Crespi, V. H.; Terrones, H.; Terrones, M. Extraordinary Room-Temperature Photoluminescence in Triangular WS_2 Monolayers. *Nano Lett.* **2012**, *13*, 3447–3454.
25. Zhao, W.; Ghorannevis, Z.; Chu, L.; Toh, M.; Kloc, C.; Tan, P.-H.; Eda, G. Evolution of Electronic Structure in Atomically Thin Sheets of WS_2 and WSe_2. *ACS Nano* **2012**, *7*, 791–797.
26. Mak, K. F.; He, K.; Shan, J.; Heinz, T. F. Control of Valley Polarization in Monolayer MoS_2 by Optical Helicity. *Nat. Nanotechnol* **2012**, *7*, 494–498.
27. Mak, K. F.; Lee, C.; Hone, J.; Shan, J.; Heinz, T. F. Atomically Thin MoS_2: A New Direct-Gap Semiconductor. *Phys. Rev. Lett.* **2010**, *105*, 136805.
28. Perea-López, N.; Elías, A. L.; Berkdemir, A.; Castro-Beltran, A.; Gutiérrez, H. R.; Feng, S.; Lv, R.; Hayashi, T.; López-Urías, F.; Ghosh, S.; *et al.* Photosensor Device Based on Few-Layered WS_2 Films. *Adv. Func. Mater.* **2013**, 10.1002/adfm.201300760.
29. Hui, Y. Y.; Liu, X.; Jie, W.; Chan, N. Y.; Hao, J.; Hsu, Y.-T.; Li, L.-J.; Guo, W.; Lau, S. P. Exceptional Tunability of Band Energy in a Compressively Strained Trilayer MoS_2 Sheet. *ACS Nano* **2013**, *7*, 7126–7131.
30. Nam, H.; Wi, S.; Rokni, H.; Chen, M.; Priessnitz, G.; Lu, W.; Liang, X. MoS_2 Transistors Fabricated *via* Plasma-Assisted Nanoprinting of Few-Layer MoS_2 Flakes into Large-Area Arrays. *ACS Nano* **2013**, *7*, 5870–5881.
31. Tsai, D.-S.; Liu, K.-K.; Lien, D.-H.; Tsai, M.-L.; Kang, C.-F.; Lin, C.-A.; Li, L.-J.; He, J.-H. Few-Layer MoS_2 with High Broadband Photogain and Fast Optical Switching for Use in Harsh Environments. *ACS Nano* **2013**, *7*, 3905–3911.
32. Huang, X.; Zeng, Z.; Zhang, H. Metal Dichalcogenide Nanosheets: Preparation, Properties and Applications. *Chem. Soc. Rev.* **2013**, *42*, 1934–1946.
33. Yin, Z.; Li, H.; Li, H.; Jiang, L.; Shi, Y.; Sun, Y.; Lu, G.; Zhang, Q.; Chen, X.; Zhang, H. Single-layer MoS_2 phototransistors. *ACS Nano* **2012**, *6*, 74–80.
34. Lopez-Sanchez, O.; Lembke, D.; Kayci, M.; Radenovic, A.; Kis, A. Ultrasensitive Photodetectors Based on Monolayer MoS_2. *Nat. Nanotechnol.* **2013**, *8*, 497–501.
35. Hu, P.; Wang, L.; Yoon, M.; Zhang, J.; Feng, W.; Wang, X.; Wen, Z.; Idrobo, J. C.; Miyamoto, Y.; Geohegan, D. B.; *et al.* Highly Responsive Ultrathin GaS Nanosheet Photodetectors on Rigid and Flexible Substrates. *Nano Lett.* **2013**, *13*, 1649–1654.
36. Lei, S.; Ge, L.; Liu, Z.; Najmaei, S.; Shi, G.; You, G.; Lou, J.; Vajtai, R.; Ajayan, P. M. Synthesis and Photoresponse of Large GaSe Atomic Layers. *Nano Lett.* **2013**, *13*, 2777–2781.
37. Hu, P.; Wen, Z.; Wang, L.; Tan, P.; Xiao, K. Synthesis of Few-Layer GaSe Nanosheets for High Performance Photodetectors. *ACS Nano* **2012**, *6*, 5988–5994.
38. Lin, M.; Wu, D.; Zhou, Y.; Huang, W.; Jiang, W.; Zheng, W.; Zhao, S.; Jin, C.; Guo, Y.; Peng, H.; *et al.* Controlled Growth of Atomically Thin In_2Se_3 Flakes by van der Waals Epitaxy. *J. Am. Chem. Soc.* **2013**, *135*, 13274–13277.
39. Shi, W.; Ding, Y. J.; Fernelius, N.; Vodopyanov, K. Efficient, Tunable, and Coherent 0.18 5.27-THz Source Based on GaSe Crystal: Erratum. *Opt. Lett.* **2003**, *28*, 136–136.
40. Allakhverdiev, K. R.; Yetis, M. Ö.; Özbek, S.; Baykara, T. K.; Salaev, E. Y. Effective nonlinear GaSe crystal. Optical Properties and Applications. *Laser Phys.* **2009**, *19*, 1092–1104.
41. Kübler, C.; Huber, R.; Tübel, S.; Leitenstorfer, A. Ultrabroadband Detection of Multi-Terahertz Field Transients with GaSe Electro-Optic Sensors: Approaching the Mear Infrared. *Appl. Phys. Lett.* **2004**, *85*, 3360.
42. Segura, A.; Bouvier, J.; Andrés, M.; Manjón, F.; Muñoz, V. Strong Optical Nonlinearities in Gallium and Indium Selenides Related to Inter-Valence-Band Transitions Induced by Light Pulses. *Phys. Rev. B: Condens. Matt.* **1997**, *56*, 4075–4084.
43. Late, D. J.; Liu, B.; Luo, J.; Yan, A.; Matte, H. S.; Grayson, M.; Rao, C. N.; Dravid, V. P. GaS and GaSe Ultrathin Layer Transistors. *Adv. Mater.* **2012**, *24*, 3549–3554.
44. Rybkovskiy, D. V.; Arutyunyan, N. R.; Orekhov, A. S.; Gromchenko, I. A.; Vorobiev, I. V.; Osadchy, A. V.; Salaev, E. Y.; Baykara, T. K.; Allakhverdiev, K. R.; Obraztsova, E. D. Size-Induced Effects in Gallium Selenide Electronic Structure: The Influence of Interlayer Interactions. *Phys. Rev. B: Condens. Matt.* **2011**, *84*, 085314.
45. Alekperov, O. Z.; Godjaev, M. O.; Zarbaliev, M. Z.; Suleimanov, R. A. Interband Photoconductivity in Layer Semiconductors GaSe, InSe and GaS. *Solid State Commun.* **1991**, *77*, 65–67.
46. De Blasi, C.; Micocci, G.; Mongelli, S.; Tepore, A. Large InSe Single Crystals Grown from Stoichiometric and Non-Stoichiometric melts. *J. Cryst. Growth* **1982**, *57*, 482–486.
47. Gouskov, A.; Camassel, J.; Gouskov, L. Growth and Characterization of III-VI-Layered Crystals Like GaSe, GaTe, InSe, $GaeS_{1-X}Te_x$ and $Ga_xIn_{1-X}Se$. *Prog Cryst Growth Charact.* **1982**, *5*, 323–413.
48. Kuroda, N.; Munakata, I.; Nishina, Y. Exciton Transitions from Spin-Orbit Split Off Valence Bands in Layer Compound InSe. *Solid State Commun.* **1980**, *33*, 687–691.
49. Kuroda, N.; Nishina, Y. Resonant Raman Scattering at Higher M_0 Exciton Edge in Layer Compound InSe. *Solid State Commun.* **1978**, *28*, 439–443.
50. Mohite, A. D.; Gopinath, P.; Shah, H. M.; Alphenaar, B. W. Exciton Dissociation and Stark Effect in the Carbon Nanotube Photocurrent Spectrum. *Nano Lett.* **2008**, *8*, 142–146.
51. Najmaei, S.; Liu, Z.; Zhou, W.; Zou, X.; Shi, G.; Lei, S.; Yakobson, B. I.; Idrobo, J. C.; Ajayan, P. M.; Lou, J. Vapour Phase Growth and Grain Boundary Structure of Molybdenum Disulphide Stomic Layers. *Nat. Mater.* **2013**, *12*, 754–759.